NASA/TM- 1998- 208127

NONLINEAR ANALYSIS OF THE SPACE SHUTTLE SUPERLIGHTWEIGHT LO_2 TANK: PART I - BEHAVIOR UNDER BOOSTER ASCENT LOADS

Richard D. Young, Michael P. Nemeth, Timothy J. Collins, and James. H. Starnes, Jr.
NASA Langley Research Center
Hampton, Virginia 23681-0001

Presented at the 39th AIAA/ASME/ASCE/AHS/ASC Structures,
Structural Dynamics, and Material Conference

AIAA Paper No. 98-1838

Long Beach, California
April 20-23, 1998

AIAA-98-1838

NONLINEAR ANALYSIS OF THE SPACE SHUTTLE SUPERLIGHTWEIGHT LO_2 TANK: PART I - BEHAVIOR UNDER BOOSTER ASCENT LOADS

Richard D. Young*, Michael P. Nemeth†, Timothy J. Collins‡, and James H. Starnes, Jr.§
NASA Langley Research Center
Hampton, Virginia 23681-0001

Abstract

Results of linear bifurcation and nonlinear analyses of the Space Shuttle superlightweight (SLWT) external liquid-oxygen (LO_2) tank for an important early booster ascent loading condition are presented. These results for thin-walled linear elastic shells that are subjected to combined mechanical and thermal loads illustrate an important type of response mode that may be encountered in the design of other liquid-fuel launch vehicles. Linear bifurcation analyses are presented that predict several nearly equal eigenvalues that correspond to local buckling modes in the forward ogive section of the LO_2 tank. In contrast, the nonlinear response phenomenon is shown to consist of short-wavelength bending deformations in the forward ogive and barrel sections of the LO_2 tank that grow in amplitude in a stable manner with increasing load. Imperfection sensitivity analyses are presented that show that the presence of several nearly equal eigenvalues does not lead to a premature general instability mode for the forward ogive section. For the linear bifurcation and nonlinear analyses, the results show that accurate predictions of the response of the shell generally require a large-scale, high-fidelity finite-element model. Results are also presented that show that the SLWT LO_2 tank can support loads in excess of approximately 2.6 times the values of the operational loads considered.

Introduction

The International Space Station (ISS) is currently planned to occupy a 51.6° orbit. Construction of the ISS will require the Space Shuttle to deliver a large number of payloads to this high-inclination orbit. However, achieving this orbit requires that the payload capacity of the orbiter be reduced by approximately 10,000 lb. To recover part of this lost payload capacity, and to minimize the number of Space Shuttle flights needed to build the ISS, the National Aeronautics and Space Administration (NASA) is developing a new lightweight external fuel tank for the Space Shuttle. This new design, referred to as the superlightweight external tank (SLWT), is made primarily of an aluminum-lithium alloy and is expected to weigh approximately 58,000 lb, which is approximately 8,000 lb lighter than the aluminum external tank currently in service. This 8,000 lb weight savings translates into an 8,000 lb increase in the payload capacity for the orbiter.

An important consideration in the design of the SLWT is the nonlinear behavior of its thin-walled regions that experience compressive or shear stresses, and the sensitivity of this behavior to initial geometric imperfections. Small initial geometric imperfections are known to sometimes cause premature buckling of thin shell structures. These effects are very important in the present study because local or global buckling of the SLWT shell wall could lead to catastrophic structural collapse or cause the thermal protection system (TPS) to separate from the tank, which could also cause the vehicle to fail. To eliminate shell-wall instabilities for operational loads, accurate predictions of the nonlinear response and imperfection sensitivity of the SLWT are needed. However, obtaining this information is a significant task. For example, accurate predictions of the nonlinear response of the SLWT have been shown in Ref. 1 to require a large-scale, high-fidelity finite element model to represent the complex structural details of the SLWT and a robust nonlinear shell analysis capability that can predict local and general instability buckling modes.

One thin-walled component of the SLWT that experiences significant compressive stresses is the liquid-oxygen (LO_2) tank (see Fig. 1). Prior to launch, the weights of the liquid-hydrogen (LH_2) tank, the LO_2 tank, and the fuel are reacted at the solid-rocket-booster attachment points, which causes meridional compressive stresses and shear stresses that extend into the nose of the SLWT. The nonlinear behavior of the SLWT LO_2 tank subjected to two critical prelaunch loading conditions has been documented extensively in Ref. 1. The tank also experiences similar compressive and shear stresses during ascent, before the two solid rocket boosters

* Aerospace Engineer, Structural Mechanics Branch. Member, AIAA.
† Senior Research Engineer, Structural Mechanics Branch. Associate Fellow, AIAA.
‡ Aerospace Engineer, Structural Mechanics Branch.
§ Head, Structural Mechanics Branch. Fellow, AIAA.

(SRBs) are jettisoned. After the SRBs are jettisoned, and prior to orbital insertion, the LO_2 tank experiences compressive stresses in the aft end of the tank instead of in the nose region.

The present paper presents results of linear bifurcation and nonlinear analyses of the LO_2 tank that were conducted at the NASA Langley Research Center. The results are for a critical flight loading condition that occurs 69.66 seconds into the flight, during ascent, before the SRBs are jettisoned (referred to herein as the early booster ascent loading condition). First, an overview of the SLWT structure and the details of the loading condition are presented. Then, details of the finite-element models, mesh convergence studies, and load simulation are summarized. Next, details of the linear bifurcation analyses are presented, and then results of nonlinear analyses for geometrically perfect and imperfect linear elastic shells are presented. The imperfection sensitivity results include a discussion of the effects of modal interactions associated with several nearly equal eigenvalues. Finally, generic aspects of the finite-element model, analyses, and results that may be applicable to the design of future liquid-fuel launch vehicles are discussed.

Overview of the Structure

The Space Shuttle consists of the orbiter, two SRBs, and the external tank (ET), as shown in Fig. 1. The ET consists of a LO_2 tank, a LH_2 tank, and an intermediate structure called the intertank (Fig. 1). The intertank transmits the weight of the fuel, the ET structural weight, and the orbiter weight to the SRBs prior to launch, and transmits thrust loads from the SRBs and the orbiter to the ET during ascent. The SLWT LO_2 tank is a thin-walled monocoque shell that is made primarily of 2195 aluminum-lithium alloy. The LO_2 tank is approximately 49.4 ft long and has a maximum diameter of approximately 27.6 ft, as indicated in Fig. 2. The LO_2 tank consists of a forward ogive section made from eight gore panels, an aft ogive section made from 12 gore panels, a cylindrical barrel section made from four barrel panels, and an aft elliptical dome section made from 12 gore panels. The coordinate systems used to locate the elements of the LO_2 tank and the intertank are also shown in Fig. 2. The coordinates (XT, Y, Z) are typically referred to as the global coordinate system of the ET, and axial positions along the tank are indicated by the coordinate value of XT in units of inches. For example, the location of the junction between the forward and aft ogive sections is indicated by writing XT = 536.74 in. Cylindrical coordinates are also used and are given by (XT, r, θ), where a positive value of θ is measured from the positive Z-axis toward the positive Y-axis, as shown in Fig. 2b.

The LO_2 tank also has a forward ring frame with a "T"-shaped cross section that is referred to herein as the T-ring frame, and an aft ring frame with a "Y"-shaped cross section that is referred to herein as the Y-ring frame. These two ring frames support a baffle assembly that prevents the fuel from sloshing during ascent. The slosh baffle, a lightweight (approximately 455 lb), thin-walled structure, is supported by deep, thin-walled rings at each end that attach to the forward T-ring and the aft Y-ring frames. Other parts of the LO_2 tank include a nonstructural nose cone, a forged forward ogive fitting and cover plate, an aft spherical dome cap that contains the LO_2 suction fitting and a covered manhole, and a vortex

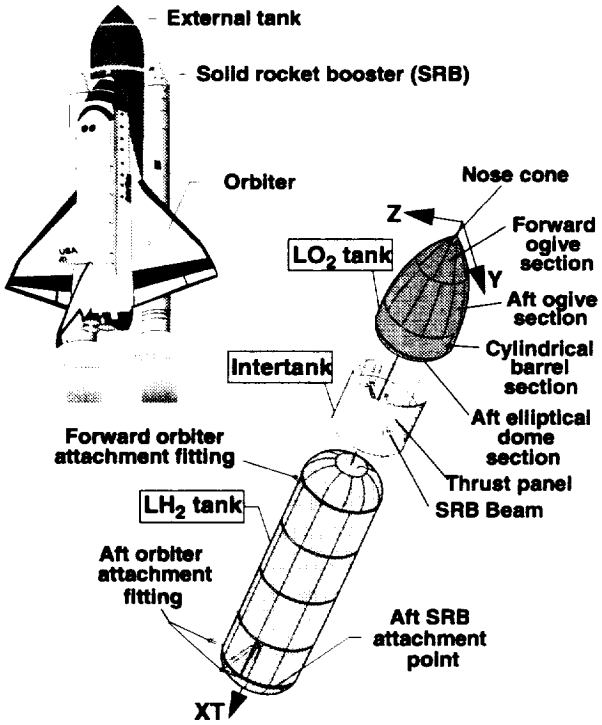

Fig. 1 Space Shuttle External Tank components.

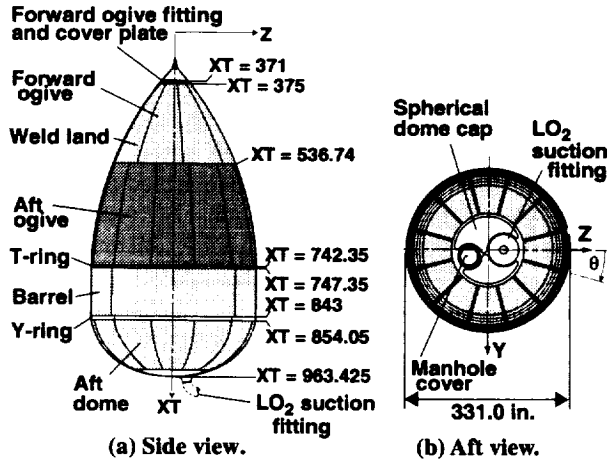

Fig. 2 Space Shuttle External LO_2 Tank components (values of XT given in inches).

baffle attached to the base of the aft dome cap. The LO_2 tank gore and barrel panels are stretch formed, chemically milled, and then welded together. The panels are fabricated with substantial thickness tailoring to reduce structural weight. The panels are somewhat thicker at the welds to form a stiffener-like region that is used as a weld land. The primary role of the weld lands is to compensate for any reduction in shell-wall strength that is caused by welding. Tapering the weld lands in thickness and width along their length reduces weight and alleviates stress concentrations in the shell that result from abrupt changes in thickness.

The intertank is a right circular cylinder that is made from 2090 aluminum-lithium and 7075 aluminum alloys and is shown in Fig. 1. The approximately 22.5-ft-long intertank has a diameter of approximately 27.5 ft and consists of six 45° curved panels that are stiffened longitudinally with external hat stiffeners and are referred to herein as skin-stringer panels. The intertank also has two massive 45° curved panels, referred to as thrust panels (see Fig. 1), that are located perpendicular to the Y-axis of the intertank and stiffened longitudinally with integrally machined external blade stiffeners. These eight panels are assembled into the intertank with mechanical fasteners and are attached to five large internal ring frames, a forward flange, and an aft flange. Longitudinal straps (referred to herein as roll ties) suppress lateral-torsional deflection of the ring frames. The main central ring frame, the thrust panels, and two thrust panel longerons are connected to each end of a tapered beam that is referred to herein as the SRB beam (see Fig. 1). The SRB beam spans the diameter of the intertank along the Y-axis and has a maximum depth (in the XT direction) of approximately 43 in. at its midspan. Forged fittings (referred to herein as SRB thrust fittings) that are incapable of transmitting moments are fastened to the ends of the SRB beam. The primary role of the thrust panels is to diffuse the large axial loads introduced by the SRBs into the intertank and then into the LO_2 tank shell wall. The SRB beam compensates for the eccentricity of the concentrated loads introduced by the SRBs. The SRB beam also supports loads that are normal to the intertank (parallel to the SRB beam) at the SRB attachment points. The intertank also has a 46-in.-high by 52-in.-wide frame-reinforced nonstructural access door located along the cylinder generator at approximately $\theta = 146°$.

Critical Loading Condition

The early booster ascent loading condition was identified by the members of the SWLT team at the NASA Marshall Space Flight Center and the Lockheed Martin Manned Space Systems Company as a critical loading condition that could cause buckling of the forward ogive of the LO_2 tank. This critical loading condition occurs 69.66 seconds into flight and corresponds to a LO_2 tank that is approximately seven-eighths full and an acceleration field given by a_X = -2.011g, a_Y = -0.049g, and a_Z = -0.440g, where g is the magnitude of the gravitational acceleration. The X subscript in the first acceleration component corresponds to the XT direction and is used in the present paper for convenience. Details of this loading condition are shown in Figs. 3 through 6. The loads, shown schematically in Fig. 3, consist of the inertial loads of the structural mass and the LO_2 mass, the ullage pressure present inside the LO_2 tank, the aerodynamic pressure distribution on the exterior surfaces of the ET, the LH_2 tank interface force and moment, and the thermal load associated with the cryogenic fuel and aerodynamic heating. The inertial loads of the structural mass are given by $m_s\, a_X$ = 54.14 kips, $m_s\, a_Y$ = 1.32 kips, and $m_s\, a_Z$ = 11.85 kips. Similarly, the inertial loads of the LO_2 mass are given by $m_{LO2}\, a_X$ = 2,466.05 kips, $m_{LO2}\, a_Y$ = 60.14 kips, and $m_{LO2}\, a_Z$ = 539.98 kips. The interface force and moment between the intertank and the LH_2 tank are given by $\mathbf{F}$ = 350.36**i** - 30.85**j** -107.73**k** kips and $\mathbf{M}$ = 2,984.87**i** - 114,288.32**j** + 16,023.38**k** in-kips, where **i**, **j**, and **k** are standard orthonormal base vectors associated with the XT, Y, and Z axes, respectively. The forces, $\mathbf{R_1}$ and $\mathbf{R_2}$, shown in Fig. 3, are the resultant forces at the SRB attachment points necessary to equilibrate all of the other loads on the structure.

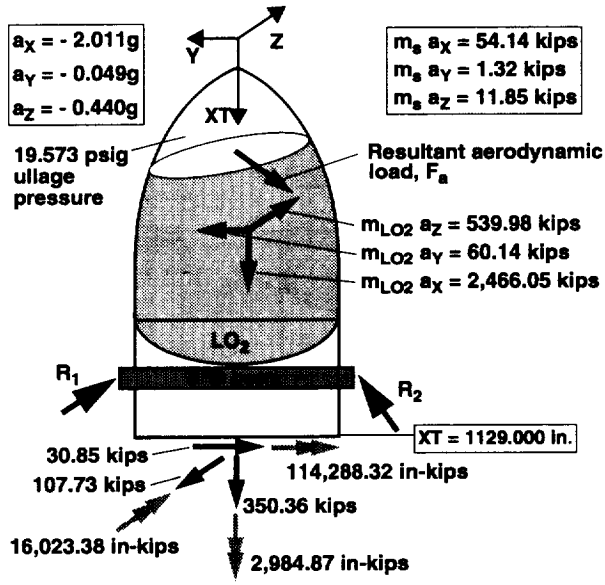

Fig. 3 Loads at 69.66 seconds into flight.

As the ET is accelerated, the LO_2 mass exerts pressure on the interior surface of the LO_2 tank shell wall. The resultant force of this pressure distribution corresponds to the inertial loads of the LO_2 that are given in Fig. 3. The pressure from the LO_2 mass and the ullage

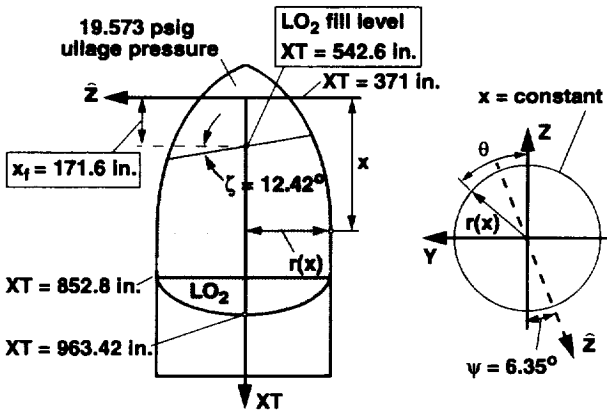

Fig. 4 LO_2 pressure distribution at 69.66 seconds into flight.

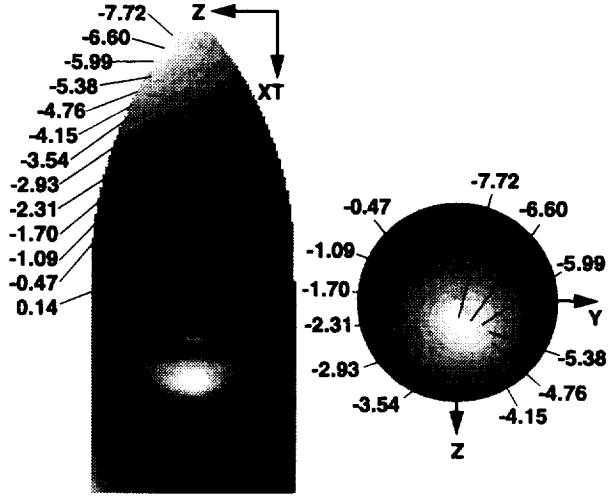

Fig. 5 Aerodynamic pressure distribution at 69.66 seconds into flight (values given in psi).

pressure are superimposed and the resulting pressure distribution on the interior surface of the LO_2 tank is approximated by the situation depicted in Fig. 4 in which the LO_2 and its container are subjected to rigid-body motion and flow effects are neglected. This approximate pressure distribution on the interior surface of the LO_2 tank is given by

$$p(x,\theta) = p_u \text{ for } x \le x_f - r(x)\left(\frac{a_Y}{a_X}\sin\theta + \frac{a_Z}{a_X}\cos\theta\right)$$

and

$$p(x,\theta) = p_u - \gamma_{LO2}\left[\frac{a_X}{g}(x - x_f) + r(x)\left(\frac{a_Y}{g}\sin\theta + \frac{a_Z}{g}\cos\theta\right)\right]$$

for $x > x_f - r(x)\left(\frac{a_Y}{a_X}\sin\theta + \frac{a_Z}{a_X}\cos\theta\right)$ where x is a local axial coordinate that is measured from XT = 371.00 in., x_f = 171.6 in. is the local x-coordinate of the fill level (XT = 542.60 in.), and r(x) is the horizontal or polar radius of the tank. The ullage pressure is given by p_u = 9.573 psig and the specific weight of the LO_2 that was used in the present study is given by γ_{LO2} = 0.04123 lb/in^3. The local $\hat{z}$-axis shown in Fig. 4b corresponds to the direction along which the free surface of the LO_2 has a maximum inclination angle relative to the y-z plane, and is given by $\theta = 180^\circ + \psi$, where $\psi = \text{Tan}^{-1}(a_Y/a_Z) = 6.35^\circ$. Similarly, the free surface of the LO_2 has an inclination angle in the x-$\hat{z}$ plane that is given by $\zeta = \text{Tan}^{-1}[\sqrt{a_Y^2 + a_Z^2}/|a_X|] = 12.42^\circ$.

The aerodynamic pressure distribution on the exterior surfaces of the ET (all surfaces except the LO_2 tank aft dome section) was approximated by interpolating a grid of known pressure values given at specific (XT, θ) coordinates. The aerodynamic pressure distribution for the early booster ascent loading condition is shown in Fig. 5, where negative values correspond to inward pressure.

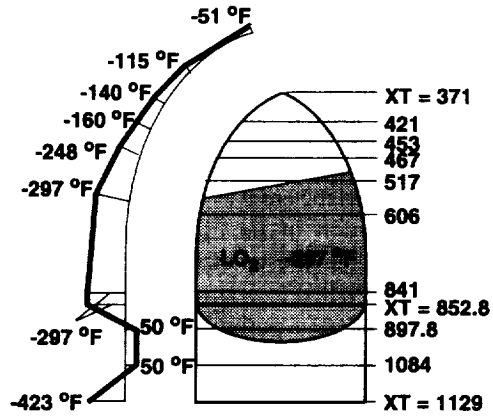

Fig. 6 Axisymmetric temperature profile at 69.66 seconds into flight (values of XT are given in inches).

The temperature distribution that was used in the present study as an approximation associated with the cryogenic fuel and aerodynamic heating is shown in Fig. 6. The temperature distribution shown in this figure is axisymmetric and varies along the surface meridians in a piecewise-linear manner. The warmest place on the LO_2 tank is the tip of the ogive section (-51 °F), and the coldest is the barrel and the aft dome sections (-297 °F). The coldest place on the intertank is at the LH_2 tank interface, given by XT = 1129 in. (-423 °F). The nominal ambient temperature of the LO_2 tank and the intertank prior to fueling is 50 °F. This temperature was used in the present study as the temperature at which thermal stresses in the LO_2 tank are absent.

Analysis Code and Finite-Element Modeling

The results of the linear bifurcation buckling and nonlinear analyses were obtained with the STructural Analysis of General Shells (STAGS) nonlinear structural analysis code for general shells.[2] The finite-element models of the SLWT tank that were used in the present study are very complex and include many structural details and the skin thickness variations or tailoring used to reduce structural weight. A detailed description of these models is presented in Refs. 1 and 3. STAGS was chosen for analyzing the SLWT tank because of its robust state-of-the-art nonlinear-equation solution algorithms and its general user-input capability that is convenient for modeling branched shells typically used for launch vehicles. In particular, STAGS uses both the full and modified Newton methods to obtain an accurate and efficient nonlinear solution, and large rotations in the shell are represented by a co-rotational algorithm at the element level. The Riks arc-length projection method is used to continue a solution past limit points. STAGS permits complex geometries, loading conditions, and initial geometric imperfections to be modeled in a direct manner by the use of user-written subroutines that are essentially independent of the mesh discretization. For example, these user-written subroutines allow the user to define reference surface geometries, tapered shell walls and stiffener cross-sections; and complex nodal force, temperature, and pressure distribution functions in a direct manner, using the FORTRAN computer language. This feature greatly simplified the definition of the finite-element models and the mesh convergence studies conducted in the present study. A description of how the features of STAGS were used in the present study to model the SLWT LO_2 tank and intertank, and details of how applied prelaunch loads were simulated are presented in Refs. 1 and 3.

The basic approach used in the present study to simulate the actual early booster ascent loading condition is to apply all loads, accelerations and associated inertial and LO_2 pressure loads illustrated in Figs. 3 and 4 to the model, except for the SRB interface loads. The nodes on the ends of the SRB beam, where the SRB forces act (see Fig. 4), were restrained so that the SRB interface forces become reactions and rigid body motion is eliminated. The thermal load was applied by introducing the axisymmetric temperature distribution shown in Fig. 6 as a temperature change from a nominal initial uniform temperature of 50°F. The applied loads were separated into two groups. The first group contains the pressure that acts on the shell wall because of the acceleration of the LO_2 mass, the structural-mass inertial loads, the inertial line loads that represent the acceleration of the slosh baffle mass that is located inside of the barrel section of the LO_2 tank, the aerodynamic pressure, and the LH_2 tank interface force and moment. This group of loads is treated as the primary source of destabilizing compressive stresses in the LO_2 tank that may occur at load levels greater than the corresponding operational load level. The second group of loads consists of the thermal load and the LO_2 tank ullage pressure. The loads in the second group are considered to be passive loads when determining the stability margin of safety of the LO_2 tank, and are constant in value throughout the analyses. In performing linear bifurcation buckling and nonlinear analyses with STAGS, two load factors, p_a and p_b, were assigned to the first (active) and second (passive) load groups, respectively. Values of $p_a = p_b = 1$ correspond to the loading condition that was described previously as the operational load level.

In modeling the SLWT LO_2 tank and the intertank, several assumptions were made to simplify the finite-element models. Limited parametric studies were conducted to determine the adequacy of the assumptions and simplifications. For each case in these studies, the modeling assumptions used to simplify the finite-element models were found to be acceptable for analyzing the nonlinear behavior of the SLWT LO_2 tank. In addition, the finite-element modeling approach that was used for the SLWT LO_2 tank was also applied for the analysis of two full-scale structural tests that were conducted at the NASA George C. Marshall Spaceflight Center on the original standard weight ET during the development program of the original Space Shuttle ET. The analytical results for these two test articles, which buckled unexpectedly during the tests, indicate that the finite-element modeling approach that is used in the present study is adequate for representing the nonlinear behavior of the SLWT LO_2 tank.[1]

Results and Discussion

Three different finite element models were used in the present study for analysis of the LO_2 tank subjected to the early booster ascent loading condition. As a first step toward identifying an adequate model with as few degrees of freedom as necessary, linear bifurcation buckling analyses were conducted. The passive loads associated with load factor p_b were applied to the STAGS models as a linear prebuckling stress state ($p_b = 1$) and the active (destabilizing) loads associated with load factor p_a were used to obtain the minimum eigenvalue. The models that were investigated had 49,000, 96,000, and 125,000 degrees of freedom. The model that was identified as adequate for predicting the linear bifurcation buckling behavior is shown in Fig. 7 and corresponds to 125,000 degrees of freedom.

The first linear bifurcation mode (referred to herein as the linear bifurcation buckling mode) for the geometrically perfect shell is shown in Fig. 8 for the STAGS model with 125,000 degrees of freedom. The eigenvalue for this model corresponds to active loads that are approximately

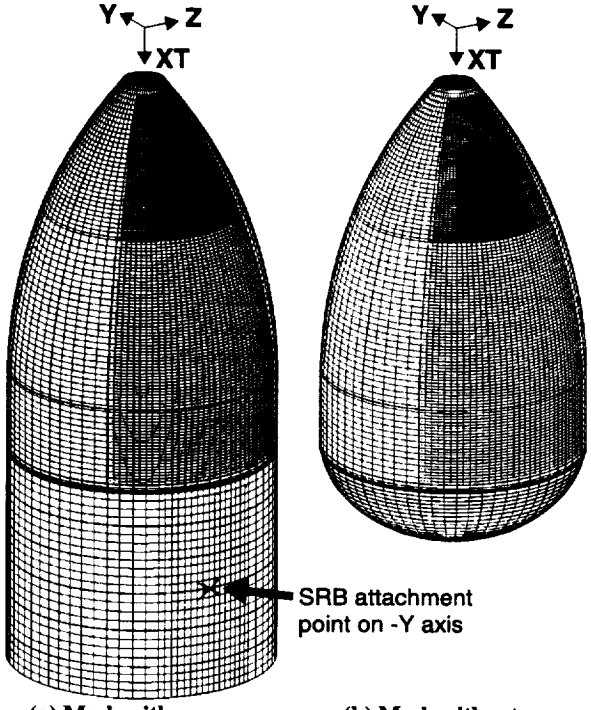

(a) Mesh with intertank shown. **(b) Mesh without intertank shown.**

Fig. 7 Finite element mesh (125,000 degrees of freedom).

2.182 times the magnitude of the corresponding operational loads shown in Figs. 3, 4 and 5. This buckling mode is a localized, short-wavelength wrinkle in the aft part of the forward ogive that extends from approximately XT = 447.31 in. to 511.87 in. and is centered circumferentially on $\theta = 267.2^{o}$ (near the negative Y-axis). The second through eighth linear bifurcation modes are also localized, short-wavelength modes, similar to the mode shown in Fig. 8, with eigenvalues equal to 2.183, 2.207, 2.209, 2.244, 2.246, 2.260, and 2.260, respectively, which are all less than 4% higher than the lowest eigenvalue. The second through sixth linear bifurcation modes are also in the aft part of the forward ogive and centered on $\theta = 267.2^{o}$. The seventh and eighth modes are located in the aft part of the forward ogive, but are on the opposite side of the tank (near the positive Y-axis) and centered on $\theta = -2.8^{o}$.

The nearly equal values of the first eight eigenvalues, the short wavelength of the linear bifurcation modes, and the locations of the linear bifurcation modes led to the dense mesh refinement of the forward ogive that is shown in Figs. 7 and 8. The mesh refinement which is shown centered on the negative Y-axis was also applied on the positive Y-axis side of the model. Meridional and circumferential mesh refinement of the forward ogive, aft ogive, and barrel sections was facilitated by the use of the five-node and seven-node rectangular transition elements available in STAGS.[3] The 96,000- and 125,000-degree-of-freedom models have the same general mesh arrangement shown in Fig. 7, but the level of refinement of the aft part of the forward ogive shown in Figs. 7 and 8 for the 125,000-degree-of-freedom model is essentially twice that of the 96,000-degree-of-freedom model. The lowest eigenvalues for the 96,000- and 125,000-degree-of-freedom models are given by $p_a = 2.204$ and $p_a = 2.182$, respectively. The smoothness of the buckling mode shown in Fig. 8 and the one-percent difference in the eigenvalues, indicate that the 125,000-degree-of-freedom model is adequate for representing the linear bifurcation behavior of the LO_2 tank for this loading condition. The 96,000- and 125,000-degree-of-freedom models were also used to obtain nonlinear solutions for geometrically perfect and imperfect shells. These solutions, which are in good agreement, indicate that the 125,000-degree of freedom model adequately represents the nonlinear behavior of the LO_2 tank for this loading condition. Thus, all subsequent results presented in this section were obtained with the 125,000-degree-of-freedom model.

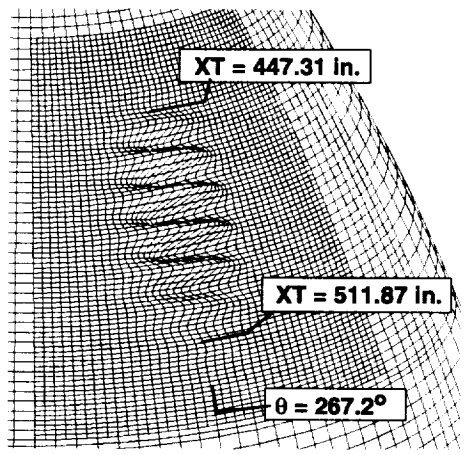

Fig. 8 Linear bifurcation buckling mode (125,000 degrees of freedom; $p_a = 2.182$ and $p_b = 1.0$).

The meridional stress resultant distribution in the LO_2 tank (on the negative Y-axis side of the tank, and given in units of lb/in.), that was obtained from nonlinear analyses, is shown in Fig. 9 for values of $p_a = p_b = 1$, and for $p_a = 2.216$ and $p_b = 1$. The darker shading shown in the figure corresponds to meridional tension which primarily resists the axial acceleration of the LO_2 mass. The lighter shading shown in the figure corresponds to meridional compression resulting from the SRB interface loads (reaction forces) which are applied in the intertank and dissipate into the LO_2 tank along the (+Y) and (-Y) axes. The highest values of meridional compression are in the aft end of the barrel near $\theta = 90^{o}$ and $\theta = 270^{o}$. The average shell wall thickness in and around this region is 0.381 in. These results show that the meridional stress in the location of the buckling modes is tensile for $p_a = 1$, but at the higher load value the meridional stress becomes compressive in the forward ogive in a region where the

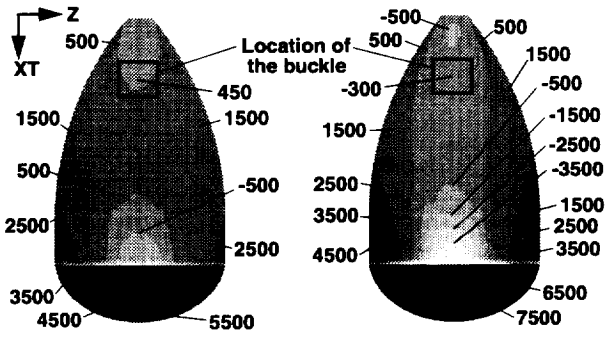

(a) $p_a = p_b = 1.0$. (b) $p_a = 2.216$ and $p_b = 1.0$.

Fig. 9 Meridional stress resultants in LO_2 tank (lb/in.).

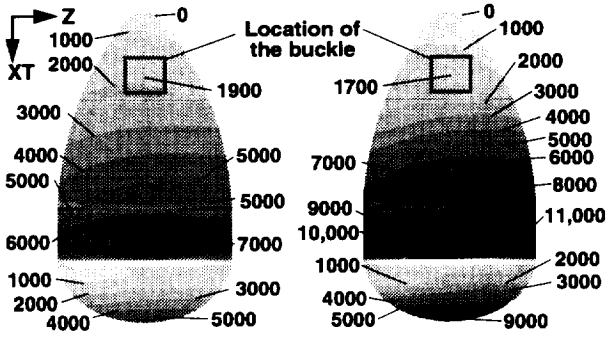

(a) $p_a = p_b = 1.0$. (b) $p_a = 2.216$ and $p_b = 1.0$.

Fig. 10 Circumferential stress resultants in LO_2 tank (lb/in.).

average wall thickness is 0.093 inches, and this meridional compression causes this region to buckle. The circumferential stress resultants in the LO_2 tank are shown in Fig. 10 for values of $p_a = p_b = 1$, and for $p_a = 2.216$ and $p_b = 1$. These results show the entire LO_2 tank exhibits circumferential tension which resists primarily the LO_2 pressure and ullage pressure. The circumferential tension, which has a stabilizing effect on the shell, is smallest in the forward ogive. The small circumferential tension in the location of the buckling mode, combined with the meridional compression, is responsible for the shortness of the wavelength of the eight linear bifurcation modes.

An important concern that arose during the course of the present study is the possibility of high sensitivity to initial geometric imperfections, that may be affected by the presence of nearly equal eigenvalues of the linear bifurcation modes. This sensitivity could lead to a premature collapse mode of the forward ogive. To address imperfection sensitivity, nonlinear analyses were conducted of an imperfect shell with an imperfection shape in the form of a linear combination of the first eight linear bifurcation modes, described previously in the present paper. Mathematically, this set of modes can be viewed loosely as a basis for an "isotropic imperfection space," similar to a basis of a vector space. The linear bifurcation modes were selected because they represent configurations that the structure has an intrinsic affinity to deform into, provided that there are no substantial nonlinear prebuckling effects present. That is, in the absence of substantial nonlinear prebuckling effects, the linear bifurcation eigenvalues represent when (at what load level) and where (what configurations) strong interactions between compressive membrane stresses and normal displacements are likely to be present. In addition, the eight-mode imperfection was selected because of the statement given by Bushnell[4] that suggests that premature failure of shell structures that exhibit a short-wavelength response can be activated or "triggered" by imperfections with a similar short-wavelength shape. Thus, the eight-mode imperfection is expected to represent adequately a preferred direction of departure from the primary equilibrium path should the structure have a tendency to do so.

Results are presented in Figs. 11, 12 and 13 that show the nonlinear deformations that were obtained from STAGS analyses of a geometrically perfect shell and a geometrically imperfect shell with an imperfection-amplitude-to-wall-thickness ratio $A/t_1 = 1$, respectively. The thickness t_1 in the ratio A/t_1 is the average wall thickness of the forward ogive where the buckling mode is located ($t_1 = 0.093$ in.). The results shown in these three figures are for nonlinear solutions that were obtained by increasing the load factors p_a and p_b simultaneously to a value of one, and then holding p_b constant while increasing the magnitude of the load factor p_a. The exaggerated deformed shape of the LO_2 tank obtained from nonlinear analysis of a geometrically perfect shell with the load factors $p_a = 2.743$ and $p_b = 1.0$ is shown in Fig. 11. The load level for this solution is approximately 2.74 times the operational load level, and approximately 1.26 times the linear bifurcation buckling load level. The deformed shape shown in Fig. 11 displays a short-wavelength bending response in the forward ogive and a bending response with a longer wavelength in the barrel. The bending deformations are present near the (+Y) and (-Y) axes ($\theta = 90°$ and 270°, respectively), but are largest for $\theta \approx 270°$. In Fig. 11, local x-coordinates, x_1 and x_2, and nondimensional normal displacements, w_1/t_1 and w_2/t_2, are defined in the forward ogive and barrel sections, respectively. The normal displacements are normalized by the average wall thickness in the region where the bending deformation occurs; i.e., $t_1 = 0.093$ in. in the forward ogive and $t_2 = 0.381$ in. in the barrel.

Results are presented in Fig. 12 that show the nondimensional normal displacements of the geometrically perfect shell along a meridian for values of the load factor p_a equal to 1.0, 2.5, and 2.743. The nondimensional normal displacements along a meridian of the forward ogive shell wall at $\theta = 267.2°$ are represented by the solid lines in Fig. 12a. Overall, negative values of the

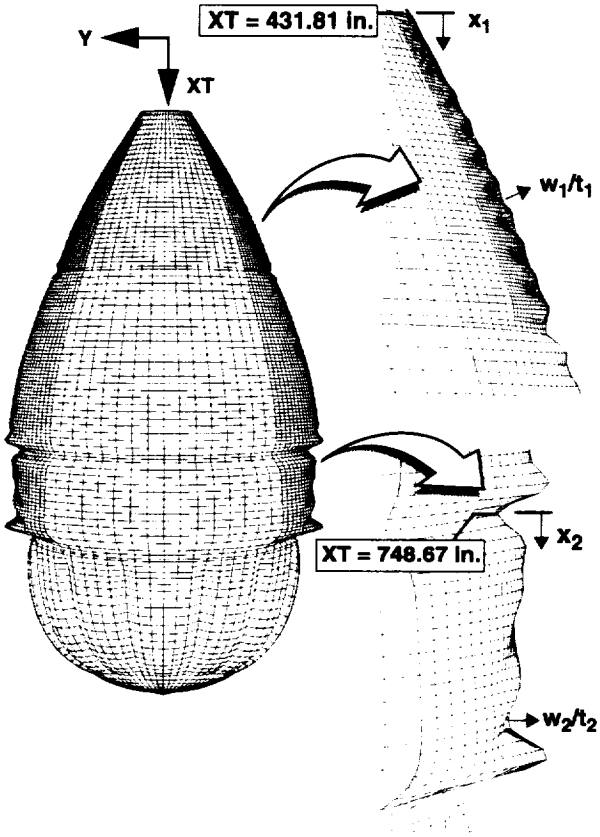

Fig. 11 Deformed shape of LO_2 tank from nonlinear analysis of geometrically perfect shell ($p_a = 2.743$, $p_b = 1.0$).

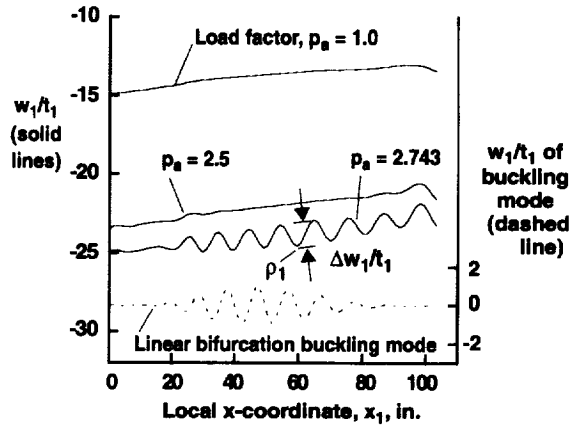

(a) Forward ogive ($t_1 = 0.093$ in.; $\theta = 267.2°$).

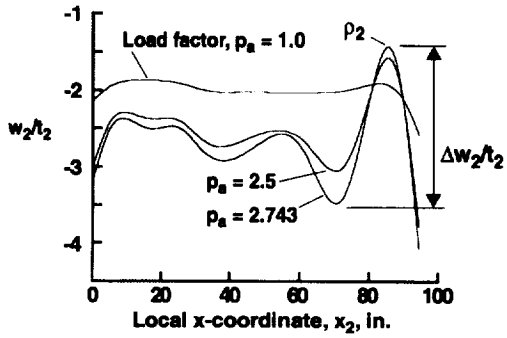

(b) Barrel ($t_2 = 0.381$ in.; $\theta = 270.0°$).

Fig. 12 Nondimensional normal displacement w/t of geometrically perfect shell; forward ogive and barrel sections.

normal displacements are indicated by the left-hand ordinate for these three load factors. These results are negative because of the LO_2 thermal load (shrinkage), and meridional compression and cross-sectional ovalization of the ET caused by the LO_2 pressure load and the discrete SRB interface loads, respectively. The linear bifurcation buckling mode is represented by the dashed line in Fig. 12a, with the normalized amplitude given by the right-hand ordinate of the figure. The nondimensional normal displacements along the meridian of the barrel shell wall at $\theta = 270.0^o$ for the three values of the load factor are shown in Fig. 12b.

The solid lines shown in Fig. 12a indicate development of a short-wavelength bending response in the forward ogive. At the operational load level given by $p_a = 1$, the results predict minimal bending deformations. At a load level of $p_a = 2.5$, which is greater than the linear bifurcation buckling load level ($p_a = 2.182$), the results predict the onset of a nonlinear bending response in the locations given by $x_1 = 25$ in. and $x_1 = 100$ in. As the load is increased to $p_a = 2.743$, substantial bending deformations (indicated by the waviness in the curves) develop and grow in the forward ogive, which reduces the apparent meridional stiffness of the forward ogive. The pattern of the nonlinear deformation is very similar to the linear bifurcation buckling mode.

The solid lines shown in the Fig. 12b indicate the development of a bending response in the LO_2 barrel with a longer wavelength than the bending response in the forward ogive. At the operational load level given by $p_a = 1$, the results predict a significant bending boundary layer at the aft end of the barrel. For $p_a = 2.5$, the results predict the nonlinear bending response has grown in amplitude and extends along the entire length of the barrel, which reduces the apparent meridional stiffness of the barrel. As the load level is increased to $p_a = 2.743$, the bending deformations in the barrel grow to an amplitude of approximately two times the average wall thickness. The bending response at the aft end of the barrel is attributed to three interacting load effects. First, the LO_2 pressure causes radially-outward bulging around the stiff joint at the intersection of the barrel, aft dome, and intertank. Second, meridional tension in the aft dome creates a moment on this joint about the circumferential coordinate line. Third, the SRB interface loads are transmitted through the intertank thrust panels and create compressive loads in the barrel at the circumferential locations centered on $\theta = 90°$ and 270° (see Fig. 9). As the load factor increas-

es, all of these loading effects increase in magnitude, and coupling between the meridional compression and the bending response causes nonlinear growth of the deformations.

Results are presented in Fig. 13 that show the nonlinear deformations in the forward ogive that were obtained from STAGS analysis of a geometrically imperfect shell with an imperfection-amplitude-to-wall-thickness ratio $A/t_1 = 1$ ($t_1 = 0.093$ in.). The eight-mode imperfection that was described previously in the present paper was used, with the imperfection shape given by -0.0325 times the summation of the first six eigenvectors, plus -0.0656 times the summation of the seventh and eighth eigenvectors. The negative-valued linear combination was used as the imperfection shape because it was found to provide a stronger nonlinear interaction with the compressive stresses in the shell wall than the positive-valued linear combination. The multiplication factors were selected to provide an imperfection shape in the forward ogive such that the regions centered on $\theta = 90°$ and 270° both had an imperfection-amplitude-to-wall-thickness ratio $A/t_1 = 1$. The nondimensional normal displacements along the meridian of the forward ogive shell wall at $\theta = 267.2°$, for values of the load factor p_a equal to 1.0, 2.5, and 2.766, are represented by the solid lines in Fig. 13. The shape of the 8-mode imperfection along the meridian at $\theta = 267.2°$ is represented by the dashed line.

The pattern of the nonlinear deformation of the geometrically imperfect ogive shown in Fig. 13 is very similar to the shape of the geometric imperfection. Comparison of the results for the geometrically perfect and geometrically imperfect forward ogive, shown by the solid lines in Figs. 12a and 13, respectively, indicates that the eight-mode imperfection greatly amplifies the severity of the bending deformation in the forward ogive and causes the growth of the bending deformations to form at

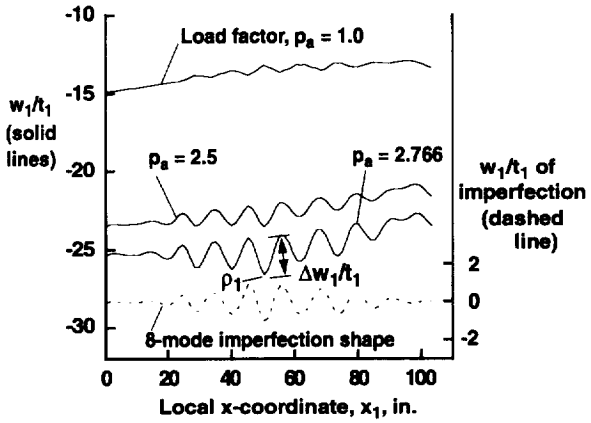

Fig. 13 Nondimensional normal displacement w_1/t_1 of geometrically imperfect forward ogive. (Imperfection-amplitude-to-wall-thickness $A/t_1 = 1$; $t_1 = 0.093$ in.; $\theta = 267.2°$).

lower load levels. The nondimensional normal displacements in the barrel of the geometrically imperfect shell are not presented, since the imperfection in the forward ogive has very little effect on the deformation in the barrel, and the results obtained are essentially the same as the geometrically perfect shell results shown in Fig. 12b.

The predicted growth of the bending deformations and the associated reductions in the apparent meridional stiffness of the forward ogive and the barrel of the geometrically perfect and imperfect shells are shown more explicitly in Fig. 14. The maximum amplitude of the undulations in the normal displacements in the forward ogive and the barrel, $\Delta w_1/t_1$ and $\Delta w_2/t_2$ (shown graphically in Figs. 12 and 13) are given as a function of the load factor p_a in Fig. 14. The two solid curves presented in Fig. 14 correspond to deformations of the forward ogive (unfilled circles) and barrel (unfilled squares) of the geometrically perfect shell. Similarly, the two dashed curves presented in Fig. 14 correspond to deformations of the forward ogive (filled circles) and barrel (filled squares) of the geometrically imperfect shell with $A/t_1 = 1$. The horizontal dashed line shown in Fig. 14 represents the linear bifurcation buckling load level ($p_a = 2.182$).

The results shown in Fig. 14 indicate that the bending deformations in the forward ogive of the geometrically perfect shell are very small for values of the load factor $p_a < 2.6$, but increase rapidly for $p_a > 2.6$. The results for the geometrically imperfect shell predict that the bending deformations in the forward ogive are negative for values of the load factor $p_a < 1.8$. These negative values correspond to flattening of the imperfection shape that is caused by tensile meridional and circumferential stresses. For $p_a > 1.8$, $\Delta w_1/t_1$ becomes positive and increases monotonically. This behavior is the result of the

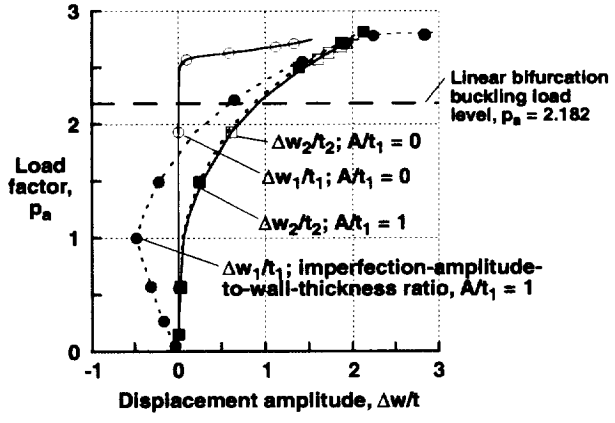

Fig. 14 Local nondimensional normal displacement amplitude, $\Delta w/t$, in forward ogive and barrel sections for geometrically perfect and geometrically imperfect forward ogive. (Forward ogive: $t_1 = 0.093$ in., for $A/t_1 = 0$, Δw_1 is at XT = 491 in., $\theta = 267.2°$; for $A/t_1 = 1$, Δw_1 is at XT = 482 in., $\theta = 267.2°$; Barrel: $t_2 = 0.381$ in., Δw_2 is at XT = 827 in., $\theta = 270.0°$).

fact that the meridional stresses in the forward ogive become compressive for $p_a > 1.8$. The results presented in Fig. 14 also predict that the bending response in the barrel ($\Delta w_2/t_2$) is small at the operational load level ($p_a = 1.0$), increases monotonically for values of the load factor $p_a > 1.0$, and is virtually unaffected by the imperfection in the forward ogive.

All the results shown in Fig. 14 generally show a monotonically increasing nonlinear response and predict that the shell can support loads greater than the buckling load predicted by a linear bifurcation analysis. As the load factor p_a increases, Δw increases (reducing the apparent meridional stiffness), and the slope of the load versus Δw curve decreases, but remains positive-valued. The reduction in slope of the load versus Δw curve indicates an increase in the rate of displacement growth, while the positive-valued slope indicates that the apparent meridional stiffness is positive-valued and that the deformation growth is stable. This type of response is similar to the response presented for the prelaunch loading condition with full LO_2 and LH_2 tanks,[1] and to the response reported by Stevens, Starnes, and Almroth[5] for cylindrical shells subjected to combined internal pressure and a pure bending moment. The results in Ref. 5 indicate that the amplitude of the short-wavelength deflection grows rapidly as the load increases and approaches a critical value. At the critical value of the load, the load-deflection response curve approaches a horizontal tangent that corresponds to a local collapse mode of the cylinder. Mathematically, the horizontal tangent indicates that unbounded growth of the displacement occurs for an infinitesimal increase in the load. It is expected that the curves shown in Fig. 14 would approach a horizontal tangent as the load factor increases until a redistribution in load occurs within the forward ogive and barrel sections. As a horizontal tangent in a load versus displacement amplitude curve is approached, the region of the shell containing the bending deformations becomes incapable of supporting additional load, and the compressive load is redistributed to another portion of the shell. If other parts of the shell cannot support the redistributed compressive load or if excessive yielding occurs, the shell will collapse.

Despite the concerns about acute imperfection sensitivity that is sometimes affected by the presence of several nearly equal linear bifurcation eigenvalues, the results presented in Figs. 12 through 14 indicate a stable nonlinear response for the imperfect shell, which has a relatively large imperfection amplitude. Moreover, the results indicate the forward ogive and barrel sections retain a positive-valued apparent meridional stiffness as the bending deformations develop, which supports the insensitivity of the collapse load to imperfections in the forward ogive. Since no eigenvectors were found that correspond to bifurcation buckling modes in the barrel, imperfection sensitivity of the barrel was not quantified. The nonlinear prebuckling deformations in the barrel were characteristic of stable growth of a bending boundary layer which is driven by the loading. The deformations in the barrel did not exhibit limit point or bifurcation type behavior, and thus should not be sensitive to imperfections. The stability of the wrinkle-like deformation states in the forward ogive and the barrel is at least partially attributed to the presence of tensile circumferential stress resultants in these regions. Furthermore, the meridional compression region is a local region that is more likely to cause a benign internal load redistribution in the presence of nonlinear prebuckling deformations than a sudden mode change or collapse. The behavior of the LO_2 tank is significantly different from that of a compression-loaded cylinder or an externally pressurized sphere which exhibit several nearly equal, or a multiplicity of, linear bifurcation eigenvalues. A major difference is that the regions of compression of the LO_2 tank do not fully envelop the shell, unlike the compression-loaded cylinder or the externally pressurized sphere. This difference facilitates load redistribution in the LO_2 tank without shell collapse or a mode change.

Although the results presented in Figs. 12 through 14 predict that the SLWT will not collapse for load levels below approximately 2.6 times the operational load level, the results also indicate that large local bending deformations may occur for loads that are much smaller than the local collapse load. These local bending deformations may cause the thermal protection system (TPS) to debond from the shell wall and fail. This mode of failure is of great importance in the design of the TPS for contemporary space vehicles. The results presented in Fig. 15 give approximate estimates of the local radii of curvature, ρ_1 and ρ_2 (identified in Figs. 12 and 13), for the bending deformation in the forward ogive and barrel sections, respectively. The local radius of curvature ρ was estimated by $\rho = |\kappa_x|^{-1}$, where κ_x is the curvature in the meridional direction of the finite element closest to the crest of the deformation pattern. The two solid curves presented in Fig. 15 correspond to bending deformations of the forward ogive (unfilled circles) and barrel (unfilled squares) of the geometrically perfect shell. Similarly, the two dashed curves presented in Fig. 15 correspond to bending deformations of the forward ogive (filled circles) and barrel (filled squares) of the geometrically imperfect shell with $A/t_1 = 1$. The results in Fig. 15 demonstrate that the geometric imperfection amplitude has a significant influence on the local radius of curvature of the forward ogive. For example, if a given thermal protection system (TPS) is known to debond from the shell wall at a value of $\rho = 100$ in., the maximum load factor before debonding occurs in the forward ogive is reduced from a value of ap-

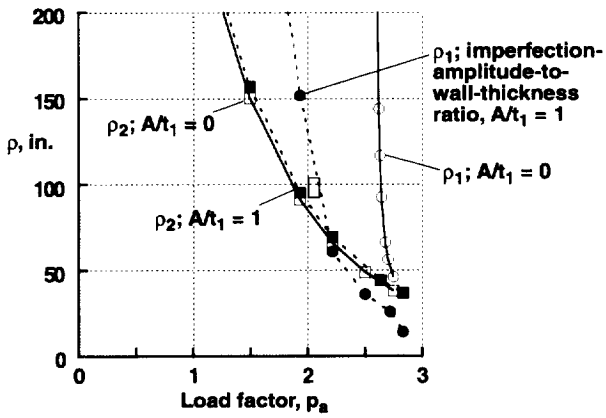

Fig. 15 Local radii of curvature ρ of bending deformation in forward ogive and barrel sections for geometrically perfect and geometrically imperfect forward ogive. (Forward ogive: t_1 = 0.093 in., for A/t_1 = 0, ρ_1 is at XT = 491 in., θ = 267.2°; for A/t_1 = 1, ρ_1 is at XT = 482 in., θ = 267.2°; Barrel: ρ_2 is at XT = 833 in., θ = 270.0°).

proximately 2.6 for the geometrically perfect shell to 2.1 for the geometrically imperfect shell with A/t_1 = 1. However, a large amplitude, short-wavelength imperfection of this type is very unlikely to be present in a piece of high-precision flight hardware. Thus, the radius-of-curvature results for the perfect shell are much more practical than the corresponding results for the imperfect shell since such large imperfections would most likely be identified during inspection of the shell. The results in Fig. 15 indicate that debonding of the TPS is more likely to first occur in the barrel. For the example given above, with an allowable ρ = 100 in., the results predict that debonding of the TPS would occur at a load factor of approximately 1.9.

Concluding Remarks

Linear bifurcation and nonlinear analyses of the Space Shuttle superlightweight (SLWT) liquid-oxygen (LO_2) tank have been presented. The loading details for an important early booster ascent loading condition have been described and the analytical method used to simulate the loading condition has been discussed. Results have been presented herein that were obtained from complex, large-scale finite-element models of a portion of the Space Shuttle SLWT. These results for thin-walled linear elastic shells that are subjected to combined mechanical and thermal loads illustrate an important type of response mode that may be encountered in the design of other liquid-fuel launch vehicles. In addition, the results indicate that large-scale, high-fidelity finite-element models are generally required to predict accurately the linear bifurcation and nonlinear responses.

For the early booster ascent loading condition, linear bifurcation analyses yielded several nearly equal eigenvalues that correspond to local buckling modes. However, the nonlinear analyses yielded a response that is characterized by short-wavelength bending deformations, in the forward ogive and barrel sections of the LO_2 tank, that grow in amplitude in a stable manner with increasing load. Imperfection sensitivity analyses have been presented that indicate that the LO_2 tank does not exhibit a nonlinear collapse mode associated with the interaction of nearly equal linear bifurcation modes in the forward ogive, for load levels below approximately 2.6 times the operational load level. However, local bending deformations may cause failure of the thermal protection system (TPS) for load levels that are less than the load level corresponding to structural collapse. To address this concern, results have been presented that can be used to estimate the load level at which TPS failure is likely to occur. The results do predict that the severity of some of the local bending deformations is significantly affected by the localized initial geometric imperfection.

Acknowledgments

The authors would like to express their thanks to Ms. V. O. Britt, Mr. Walter L. Heard, Jr., Dr. Charles C. Rankin, Mr. Michael Quiggle, and Mr. Neil Otte of Gulf Stream Aerospace, Inc., NASA Langley Research Center (retired), Lockheed Martin Missiles and Space Company, Lockheed Martin Manned Space Systems Division, and the NASA George C. Marshall Space Flight Center, respectively, for their technical support.

References

[1]Nemeth, M. P., Britt, V. O., Collins, T. J., and Starnes, J. H., Jr., Nonlinear Analysis of the Space Shuttle Superlightweight External Fuel Tank, NASA TP 3616, December, 1996.

[2]Brogan, F. A., Rankin, C. C., and Cabiness, H. D., "STAGS User Manual," Lockheed Palo Alto Research Laboratory, Report LMSC P032594, 1994.

[3]Young, R. D. and Rankin, C. C., "Modeling and Nonlinear Analyses of a Large-Scale Launch Vehicle Under Combined Thermal and Mechanical Loads," Proceedings of the 37th AIAA/ASME/ASCE/AHS/ASC Structures, Structural Dynamics, and Materials Conference, Salt Lake City, Utah, April 15-17, 1996, pp. 2023-2033. AIAA Paper No. 96-1551

[4]Bushnell, D., "Static Collapse: A Survey of Methods and Modes of Behavior," Collapse Analysis of Structures, PVP-Vol. 84, ASME, 1984, pp. 30-32.

[5]Stephens, W. B., Starnes, J. H., Jr., and Almroth, B. O., "Collapse of Long Cylindrical Shells Under Combined Bending and Pressure Loads," AIAA Journal, Vol. 13, No. 1, 1975, pp. 20-25.